



# Fracture toughness trends of modulus-matched TiN/(Cr,Al)N thin film superlattices

J. Buchinger<sup>a,\*</sup>, A. Wagner<sup>a</sup>, Z. Chen<sup>b</sup>, Z.L. Zhang<sup>b</sup>, D. Holec<sup>c</sup>, P.H. Mayrhofer<sup>a</sup>, M. Bartosik<sup>a</sup>

<sup>a</sup> Institute of Materials Science and Technology, TU Wien, Getreidemarkt 9, Vienna, A-1060, Austria

<sup>b</sup> Erich Schmid Institute of Materials Science, Austrian Academy of Sciences, Jahnstraße 12, Leoben, A-8700, Austria

<sup>c</sup> Department of Materials Science, Montanuniversität Leoben, Leoben, A-8700, Austria



## ARTICLE INFO

### Article history:

Received 2 July 2020

Revised 22 October 2020

Accepted 28 October 2020

Available online 1 November 2020

### Keywords:

Superlattice

Thin Film

Transition Metal Nitrides

Fracture Toughness

Continuum Mechanics

## ABSTRACT

Through superlattice (SL) architectures, the hardness as well as the fracture toughness of ceramic thin films can be enhanced. The hardness-related SL effect is reasonably well understood, however, the mechanisms driving the toughness-enhancing effect are still partially unexplored. To isolate the effect of the lattice mismatch from the elastic moduli mismatch on the toughness-related properties, we designed TiN/Cr<sub>0.37</sub>Al<sub>0.63</sub>N superlattices, in which the involved layers have effectively identical elastic moduli, but sizeably different lattice parameters.

Micromechanical bending tests show an enhanced fracture toughness  $K_{IC}$  of the SLs ( $2.5 \pm 0.1$  MPa $\sqrt{m}$ ) compared with monolithic TiN ( $2.0 \pm 0.1$  MPa $\sqrt{m}$ ) and Cr<sub>0.37</sub>Al<sub>0.63</sub>N ( $1.3 \pm 0.1$  MPa $\sqrt{m}$ ) with only a weak bilayer period ( $\Lambda$ ) dependence. Superimposing an analytical model based on continuum mechanics on the experimental data, we demonstrate that, at low  $\Lambda$ , the nanolayers within the SL exhibit strong coherency strains, as misfit dislocation formation is energetically unfavourable. With increasing layer thicknesses, misfit dislocations start to form in the two layer materials – first in Cr<sub>0.37</sub>Al<sub>0.63</sub>N and slightly  $\Lambda$ -shifted in TiN. The associated evolution of coherency strains in the TiN and Cr<sub>0.37</sub>Al<sub>0.63</sub>N layers causes the observed bilayer-period-dependent toughness enhancement beyond the constituent materials. Supporting structural, morphological, chemical, and mechanical analyses are provided by X-ray diffraction, electron microscopy techniques, and nanoindentation.

© 2020 Published by Elsevier Ltd on behalf of Acta Materialia Inc.

## 1. Introduction

Transition metal nitride (TMN) thin films are known to perform excellently in terms of thermal, mechanical, and chemical resistance [1–5]. However, they are commonly plagued by a critically low intrinsic fracture toughness. As a consequence of their high hardness, crack formation is a difficult process on pristine surfaces of TMNs. Propagation of a pre-existing crack through such a material, however, can be fatally easy. This might render the fracture toughness of TMNs a particularly pressing topic, nevertheless, studies on the matter are much less abundant than for other – more established – characteristics. The small number of reports on this topic can be explained by the fact that reliable testing methods for toughness-related properties of ceramic thin films on the microscale have only become available recently. Developments of micromechanical testing methods such as pillar splitting [6], and

cantilever bending tests [7–9], but also more sophisticated synergies between ab-initio calculations and experiments [10], have facilitated research, focusing on different approaches to alleviate this critical weakness of TMNs. These studies report phase transformations [11,12], grain boundary strengthening [13,14], a tilted grain boundary design [15], alloying and/or vacancy modifications on either sublattice [16–22], as well as complex nanoscaled architectures [23–28] as possible toughening mechanisms. A particularly promising strategy has been uncovered relatively recently, with the report of the toughness-enhancing superlattice (SL) effect on polycrystalline [25,29] and single-crystal SL thin films [30]. In these studies, TiN and CrN [25,29], as well as TiN and WN<sub>x</sub> [30], were combined in a superlattice architecture – a nanolayered architecture, in which the constituent materials are compositionally different, but structurally similar (as coherent growth is a central aspect of such a structure). As a result, simultaneous hardness and toughness enhancement was observed.

The superlattice arrangement has been known to provide beneficial effects for TMN thin film since at least the 1980s and the

\* Corresponding author.

E-mail address: [julian.buchinger@tuwien.ac.at](mailto:julian.buchinger@tuwien.ac.at) (J. Buchinger).

study of Helmersson et al. [31], showing that the hardness of TiN/VN SLs significantly exceeds that of their monolithic building blocks. Their results also showed a very strong dependence on the bilayer period ( $\Lambda$ ) – the cumulative thickness of two adjacent layers in a superlattice. Building upon these initial findings, Mirkarimi et al. [32], and Chu and Barnett [33] further ascertained the underlying mechanisms of the effect. The model of Chu and Barnett [33] is based on dislocation glide within individual layers, and dislocation glide across interfaces. The resistance of a TMN SL against dislocation glide within the layers increases with decreasing bilayer period, whereas glide across interfaces becomes easier, causing the characteristic hardness peak with changing bilayer period [33]. The difference in shear modulus between the individual layers of a TMN SL consequently constitutes a key factor shaping the extent of the hardness enhancement. Apart from its direct benefit for the mechanical properties of TMN thin films, the SL architecture also provides other useful effects, for instance, the stabilisation of metastable phases with exceptional properties [34–38], as well as superior tribological properties [39–43].

Contrary to the origin of the hardness-related SL effect, the mechanisms governing the toughness-enhancing effect, are yet to be fully explored. Previous studies have provided strong evidence for its existence [25,30], and have highlighted the importance of an elastic mismatch between the constituents of the superlattice for the occurrence of a pronounced – strongly bilayer-period-dependent – toughness enhancement [30]. However, the studies [25,30] have noted that the toughness enhancement can not be explained solely by elastic differences, and that structural differences (i.e. primarily the lattice mismatch between the layers) may play a central role [25].

Here, we developed TiN/Cr<sub>0.37</sub>Al<sub>0.63</sub>N SL thin films, composed of layers with effectively identical elastic moduli. This allows for isolation of the effect of the lattice mismatch between the SL layers on the toughness enhancement. Using continuum mechanics (CM), we quantified this effect by calculating the evolution of coherency strains and misfit dislocations with changing bilayer period, from which the fracture toughness of our TiN/Cr<sub>0.37</sub>Al<sub>0.63</sub>N SLs was derived. Based on the excellent agreement of the modelled and experimentally measured (using in-situ single cantilever bending tests) fracture toughness values, as well as the validation of our modelled misfit dislocation evolution via, e.g., transmission electron microscopy, we highlight the importance of the lattice mismatch for the toughness enhancement in TMN superlattices. However, our results also indicate that the elastic mismatch is crucial for obtaining a strong bilayer period dependence.

## 2. Methodology

### 2.1. Experimental

We synthesised six TiN/Cr<sub>0.37</sub>Al<sub>0.63</sub>N SL thin films with different bilayer periods (2.5, 4.0, 7.3, 8.0, 14.0, and 22.0 nm) and monolithic TiN and Cr<sub>0.37</sub>Al<sub>0.63</sub>N by unbalanced DC reactive magnetron sputtering using an AJA International Orion 5 magnetron sputtering deposition system. We used a 3" Ti target, a 2" Al<sub>0.6</sub>Cr<sub>0.4</sub>, and a 2" Al<sub>0.7</sub>Cr<sub>0.3</sub> target. The computer-controlled shutter system enabled the growth of the superlattice architecture – aiming for TiN and Cr<sub>0.37</sub>Al<sub>0.63</sub>N layers of equal thickness. The thin films were deposited on Si (100) and MgO (100) substrates, which were ultrasonically cleaned first in acetone and subsequently in ethanol for 5 min each, before being placed in the rotary substrate holder of the system. The chamber was evacuated to a base pressure of approximately 10<sup>-4</sup> Pa, followed by thermal purging at 500°C for 20 min. The Si and MgO substrates were Ar-ion-etched at a pressure of 6 Pa, and a DC potential of -750 V. All coatings were prepared in a mixed Ar/N<sub>2</sub> atmosphere (with a flow rate ratio of 5.5 sccm/4.5

sccm) at a pressure of 0.4 Pa, and a temperature of 500°C, while operating the Ti target with 400 W and the Al<sub>0.6</sub>Cr<sub>0.4</sub> and Al<sub>0.7</sub>Cr<sub>0.3</sub> targets with 175 W. The monolithic (Cr,Al)N, and the (Cr,Al)N layers within the SLs were thus co-sputtered from the two Al<sub>x</sub>Cr<sub>1-x</sub> targets. A DC bias potential of -50 V was applied to the substrates during deposition.

X-ray diffraction (XRD) in Bragg-Brentano setup, featuring Cu K $\alpha$  radiation, was performed to structurally analyse the deposited films. Their thickness and morphology were studied on fracture cross-sections using an FEI Quanta 250 FEG (a field emission gun scanning electron microscope – FEGSEM). Employing the attached EDAX Octane Elite EDS (energy-dispersive X-ray spectroscopy) system, the chemical composition of the coatings was obtained. All EDS measurements were carried out with an acceleration voltage of 20 kV and a resolution of 128 eV.

Our TiN/Cr<sub>0.37</sub>Al<sub>0.63</sub>N films were additionally investigated with regard to their microstructure and atomic structure using a JEM JEOL 2100F transmission electron microscope (TEM), operated with 200 kV, and equipped with an image-side spherical aberration corrector. The microscope was operated at a voltage of 200 kV. The cross-sectional TEM samples were prepared using a standard sample preparation approach, including grinding, polishing, dimpling, and ion-milling procedures. Scanning TEM (STEM) images were recorded using a high-angle annular dark-field (HAADF) detector with the detector inner angle/outer angle set to be 54 mrad/144 mrad.

Indentation hardness (H) and modulus (E) of our films were determined by nanoindentation [44–48], using a Fischer-Cripps Laboratories ultra-microindentation system (UMIS) – equipped with a Berkovich indenter. The presented indentation moduli are extrapolated values at a theoretical indentation depth of zero, following the procedure of [48], and the hardness was obtained from the depth-independent section of the hardness-depth plot of each sample, as described, for instance, in [46]. On each sample, 31 indentations were performed with forces ranging from 3 mN to 45 mN, and indentation curves exceeding a depth of 10% of the coating thickness were excluded from the evaluation.

The fracture toughness of our films deposited on Si (100) was determined by performing displacement-controlled bending tests on pre-notched single cantilevers of free-standing film material [8,9,49]. We removed the Si substrate below the coating at the edge of the samples, by immersing them in a 30% KOH solution (heated to 70°C) for 2 h. The cantilevers were ion-milled with an FEI Quanta 200 3D DFIB (a focussed ion beam – FIB – workstation), equipped with a Ga ion source. The ion beam current was set to 1 nA for rough milling steps, and to 500 pA for final cuts. The notches were cut with a current of 50 pA. For all FIB processes, we set the acceleration voltage to 30 kV, and targeted cantilever dimensions of thickness w, breadth b ≈ w, and length l ≈ 7w. The bending tests were conducted with a PI85 PicoIndenter (Hysitron), mounted inside the FEGSEM, and equipped with a spherical diamond tip with a tip radius of 1 μm. We loaded the cantilevers until failure with a fixed displacement rate of 5 nm/s. The maximum force at failure F<sub>f</sub>, the dimensions of the cantilevers, as well as the depth of the notch c<sub>0</sub> were all used to derive the fracture toughness in terms of the critical stress intensity K<sub>IC</sub> of the films. For this, Eqs. 1 and 2, suggested by Matoy et al. [8], were used, which are methodologically related to the work of Di Maio and Roberts [49] and optimised for our cantilever geometries. Limitations of the approach described in [49] for relatively short pentagonal cantilevers have recently been noted by Athanasiou et al. [50] and Liu et al. [51].

$$K_{IC} = \frac{F_f l}{3 bw^2} f\left(\frac{c_0}{w}\right). \quad (1)$$

Thereby,  $b$  is the breadth,  $l$  the length, and  $w$  the thickness of the cantilever.  $f(c_0/w)$  stands for the following polynomial shape function:

$$f\left(\frac{c_0}{w}\right) = 1.46 + 24.36\left(\frac{c_0}{w}\right) - 47.21\left(\frac{c_0}{w}\right)^2 + 75.18\left(\frac{c_0}{w}\right)^3. \quad (2)$$

The fracture energy  $G_C$  was calculated for plane strain conditions using the following equation:

$$G_C = \frac{K_{IC}^2(1-\nu^2)}{E}. \quad (3)$$

While  $K_{IC}$  and  $E$  values were taken from our experiments, the Poisson's ratio  $\nu$  was extracted from DFT data of TiN [30] and (Cr,Al)N [52], applying the rule of mixture for the SLs.

The deflection ( $\Delta x$ ) of the cantilevers was normalised by calculating the bending strain  $\varepsilon_b$  of the cantilevers using Eq. 4, derived from Euler-Bernoulli beam theory [53,54].

$$\varepsilon_b = \frac{3}{2} \frac{\Delta x(w - c_0)}{l^2}. \quad (4)$$

The morphology and dimensions of the resulting fracture surface were also analysed using the FEGSEM.

Lastly, experimental measurements are quoted in terms of their sample mean and standard error. For quantities derived from two or more independently measured properties (e.g.  $G_C$ ), error propagation is employed to estimate the inaccuracy of the derived quantity.

## 2.2. Continuum mechanics

We estimate the effect of the residual stress state in a SL – resulting from the lattice mismatch of the constituting layers and the formation of misfit dislocations – on its crack growth resistance. The analytical procedure is presented in detail in [55] for the TiN/CrN system. Hence, we will discuss it only briefly in the following. Calculational details pertaining specifically to the TiN/Cr<sub>0.37</sub>Al<sub>0.63</sub>N system of the present study are provided as supplementary material.

The strain energy within the layers continuously increases during growth until a critical thickness is reached, at which misfit dislocations form. Their mean distance is estimated – analogous to the concept of Frank and van der Merwe [56] – by minimising the sum of the strain energy due to the mean strain in the layer and the energy resulting from the local dislocation stress field with respect to the dislocation density. Over the years, further concepts for structural misfit accommodation have been proposed, e.g. by Matthews and Blakeslee [57]. In our face-centred cubic (B1 rock-salt-like, rs) layers, we consider a network of orthogonal edge type dislocation arrays {with Burgers (b) and line (u) vectors of  $b_1 = a/2[110]$  and  $u_1 = [1\bar{1}0]$  and  $b_2 = a/2[\bar{1}10]$  and  $u_2 = [\bar{1}10]$ } within their (001) interface plane.

Herein, the line energy of a dislocation at the interface is estimated by averaging the shear modulus  $G$  and Poisson's ratio  $\nu$  of the adjacent layers and applying the formula for the line energy of a dislocation in an isotropic infinite medium,

$$U_l^{disloc} = \frac{G \cdot b^2}{4\pi(1-\nu)} \ln\left(\frac{h_l}{r_l}\right) + U_l^{core}, \quad (5)$$

where  $h_l$  represents the thickness of layer l and  $r_l$  is the dislocation core radius which we define to be equivalent to the magnitude of the Burgers vector. We consider the dislocation core energy  $U_l^{core}$  to be 1.5eV/Å.

A biaxial stress state in the (001)-plane is considered for evaluating the strain energy due to the partly relaxed misfit strain. With

the biaxial modulus  $M_l$  [Eq. (6)], we obtained the stress-strain relations of our layers for biaxial stresses in the (001)-plane.

$$M_l = C_{11,l} + C_{12,l} - 2 \frac{C_{12,l}^2}{C_{11,l}}, \quad (6)$$

where  $C_{ij,l}$ , using Voigt's notation, are the elements of the stiffness tensor of layer l. For numerical values of  $C_{ij,l}$  and  $M_l$  see Supplementary Table 1.  $C_{ij}$  values of Cr<sub>0.37</sub>Al<sub>0.63</sub>N, TiN, and Si were taken from [52,58], and [59,60], respectively. In the simplest version of the algorithms described in [55], the substrate is considered infinitely stiff, hence, no curvature is induced.

The dislocation density  $Q_l$  in layer l for a consecutive layer deposition can be described after [55] as a recursive function, using:

$$Q_l = \frac{|a_{cl} - \hat{a}_{(l-1)}|}{\hat{a}_{(l-1)} \cdot b_x} - \frac{U_l^{disloc} \cdot a_{cl}^2}{M_l \cdot h_{cl} \cdot \hat{a}_{(l-1)}^2 b_{xl}^2}, \quad (7)$$

with

$$\hat{a}_{(l-1)} = a_s \cdot \prod_{n=1}^{l-1} \left( 1 + \frac{|a_{cn} - \hat{a}_{(n-1)}|}{a_{cn} - \hat{a}_{(n-1)}} \cdot b_{xn} \cdot Q_n \right) \quad (8)$$

and

$$\hat{a}_0 = a_s, \quad (9)$$

where  $a_{cl}$  is the inherent lattice parameter (Supplementary Table 1) and  $\hat{a}_l$  the lattice parameter after deposition of layer l;  $a_s$  is the lattice parameter of the substrate and  $b_{xl}$  is the part of the Burger's vector parallel to the interface. (Please consider that any negative value resulting from Eq. 7 must be set to zero as there is no negative dislocation density). A more precise treatment of the dislocation energy has only a minor influence on the qualitative behaviour of dislocation formation with respect to the bilayer period [55]. The in-plane stresses  $\sigma_l$ , due to the mean strain in the layer, can then be directly determined by:

$$\sigma_l = M_l \cdot \frac{\hat{a}_l - a_{cl}}{a_{cl}}. \quad (10)$$

Accumulating the piecewise constant stress distributions in the individual layers leads to the resulting residual stress profile  $\sigma_{res}(z)$  (see Supplementary Fig. 1).

The weight function theory, first proposed by Bueckner [61] and expanded by Rice [62,63], enables estimation of the stress intensity factor of an arbitrary stress distribution for a linear elastic plane problem as a function of crack length c. From this, we obtain the stress intensity factor  $K_{res}$  due to residual stresses:

$$K_{res}(c) = \int_0^c h(z,c) \sigma_{res}(z) dz, \quad (11)$$

where  $h(z,a)$  is the so-called weight function and z the distance from the surface. Issues related to the configurational stability of crack growth in general weight function theory have been addressed, for instance, by Gao and Rice [64,65]. For an edge-cracked beam with arbitrary stress distribution normal to the crack path, Fett [66] derived a weight function, suitable for our experimental set up. The fracture toughness of the system  $K_{sys}$  as a function of crack length (see Supplementary Fig. 2) is then calculated by subtracting  $K_{res}$  from the inherent critical stress intensity of the layer  $K_{IC}$ .

$$K_{sys}(c) = K_{IC}(c) - K_{res}(c). \quad (12)$$

The alternating stress fields in a free-standing SL cantilever can either increase (compressive region) or decrease (tensile region) the inherent fracture toughness of the corresponding layer. Considering a configuration, where the layer material with a lower inherent fracture toughness is under tensile stress, as in the presented

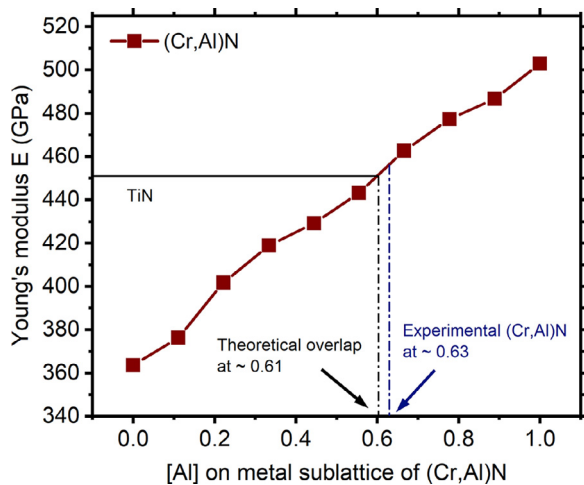


**Fig. 1.** Al-dependent DFT-based polycrystalline Young's modulus of  $(\text{Cr},\text{Al})\text{N}$ . The DFT-based polycrystalline Young's modulus of TiN (452 GPa) crosses the linear fit at  $x = 0.61$ .

SL system, a crack with its initial tip in a tensile stress region will undergo unstable crack growth until reaching the next compressive layer, followed by stable crack growth until the next local fracture toughness maximum is reached. We define this local maximum as the system's apparent fracture toughness, which we compare with the experimentally obtained fracture toughness values for different SLs.

Lastly, the TiN/ $\text{Cr}_{0.37}\text{Al}_{0.63}\text{N}$  SL system of the present study features layer materials with effectively identical coefficients of thermal expansion (CTEs) [67] within a temperature range from room temperature to 900 K. Thus, the CTE mismatch between the layers was neglected in the present model, as it influences neither the stress profile, nor the fracture toughness of TiN/ $\text{Cr}_{0.37}\text{Al}_{0.63}\text{N}$  in a measurable way.

### 3. Results and discussion

#### 3.1. Chemistry

Fig. 1, which combines DFT-calculated polycrystalline Young's moduli of  $(\text{Cr},\text{Al})\text{N}$  [52] and TiN [30], shows that the values match for an Al content,  $x$ , of 0.61 in  $\text{Cr}_{1-x}\text{Al}_x\text{N}$ . Therefore, we aimed for this chemical composition by co-sputtering  $\text{Al}_{0.6}\text{Cr}_{0.4}$  and  $\text{Al}_{0.7}\text{Cr}_{0.3}$  targets. EDS analysis of the  $(\text{Cr},\text{Al})\text{N}$  in our SLs yields values for  $x$  between 0.62 and 0.63. The EDS investigation of the monolithically prepared  $(\text{Cr},\text{Al})\text{N}$  film gives an  $x$  of 0.63. Therefore, we refer to the  $(\text{Cr},\text{Al})\text{N}$  coating and the  $(\text{Cr},\text{Al})\text{N}$  layers of our SLs as  $\text{Cr}_{0.37}\text{Al}_{0.63}\text{N}$ , which would be expected to have a Young's modulus of roughly 458 GPa, compared to the 452 GPa of TiN. The DFT-based polycrystalline shear modulus  $G$  is 191 GPa for  $\text{Cr}_{0.37}\text{Al}_{0.63}\text{N}$  and 183 GPa for TiN, with the corresponding Poisson ratios  $\nu$  being 0.21 and 0.23, respectively. The consulted studies [30,52] calculated the shear and bulk (B) moduli directly from the respective elastic constants, from which we derived the remaining elastic quantities (e.g.  $E$  and  $\nu$ ). Although the DFT-based polycrystalline elastic moduli of TiN and  $\text{Cr}_{0.37}\text{Al}_{0.63}\text{N}$  match, their directional elastic moduli differ, due to differences in the elastic constants  $C_{ij}$  of TiN [30] and  $\text{Cr}_{0.37}\text{Al}_{0.63}\text{N}$  [52]. Since explanations of the hardness-related superlattice effect in TMNs refer to shear moduli differences [33], and toughness-related trends in nanolaminated structures commonly refer to Young's moduli differences [68] of the involved layers, we regard these ( $E$  and  $G$ ) as important quantities.

The EDS-measured nitrogen concentrations in our coatings are 55 % ( $\text{Cr}_{0.37}\text{Al}_{0.63}\text{N}$ ), 59 % (TiN), and  $56 \pm 1$  % (for all SLs). Based on

this analysis, the nitrogen content appears to be relatively constant across all our samples. The values might suggest a small overstoichiometry of nitrogen in all our films, however EDS-based quantifications of light elements (e.g. nitrogen) are known to be inaccurate [69,70].

### 3.2. Structure

#### 3.2.1. X-ray diffraction

The X-ray diffraction (XRD) patterns of the monolithically grown coatings, TiN and  $\text{Cr}_{0.37}\text{Al}_{0.63}\text{N}$ , on Si (100) substrates (Fig. 2a), show a clear single-phased face-centred cubic (B1 rock-salt-like, rs) structure for both. For TiN, this is the stable equilibrium structure. Face-centred cubic  $\text{Cr}_{0.37}\text{Al}_{0.63}\text{N}$  is actually even a chemically unstable solid solution (with regard to decomposition), only realised through kinetic restrictions during the growth from the vapour phase [71,72]. The XRD pattern of  $\text{Cr}_{0.37}\text{Al}_{0.63}\text{N}$  evinces a preferred 111-orientation, as well as rather sharp Bragg peaks. The TiN film on Si (100) exhibits a more random growth orientation and the corresponding Bragg peaks are broader compared to  $\text{Cr}_{0.37}\text{Al}_{0.63}\text{N}$ . The width of Bragg peaks within single-phased materials correlates with the defect density, and larger widths typically suggest smaller grains and/or larger strains. Based on the stress-affected XRD patterns in Fig. 2a, the lattice parameters of TiN and  $\text{Cr}_{0.37}\text{Al}_{0.63}\text{N}$  on Si (100) are 4.25 Å and 4.11 Å, respectively. This constitutes a lattice mismatch of 0.14 Å, which is effectively identical to the theoretically expected value [30,52].

In Fig. 2 in general, the XRD patterns of the SL films are labelled with their bilayer period as obtained by SEM-based thickness measurements of the coatings and verified by the satellite peak positions – which are fingerprints of the superlattice architecture [73] (illustrated in Fig. 2b) – as well as detailed HRTEM studies (shown later). For the SL films with larger bilayer periods of 14.0 and 22.0 nm, the 1<sup>st</sup> ( $\pm 1$ ) and 2<sup>nd</sup> ( $\pm 2$ ) order satellite peaks are already very close to the main Bragg peaks – i.e. the 0<sup>th</sup> order peaks. Here, notable peak splitting can be observed in the patterns taken from films on Si (100) (Fig. 2a) as the TiN and  $\text{Cr}_{0.37}\text{Al}_{0.63}\text{N}$  layers are sufficiently thick to approach their unstrained lattice parameters. All SL films grown on Si (100) substrates (except the one with the smallest bilayer period of 2.5 nm) show a slightly dominant (100) growth orientation, and relatively broad Bragg peaks, indicating a finer grain size and/or larger strain than the monolithically grown films. The SL with the lowest bilayer period (~2.5 nm) shows a pronounced 111-oriented growth and Bragg peaks rather similar to the  $\text{Cr}_{0.37}\text{Al}_{0.63}\text{N}$  coating. Therefore, the 2.5 nm SL shows evidence of a larger columnar grain size than the other SLs on Si. The referential peak positions, indicated in Fig. 2a, are derived from DFT-calculated lattice parameters of rs-TiN [30], rs-CrN [52,72], and rs-AlN [58].

All films grown on MgO (100) show a pronounced 100-oriented growth, as depicted in Fig. 2b. The pronounced satellite peaks present in the patterns of the SL films are fingerprints of their high epitaxial quality, indicative of well-defined and sharp interfaces. On MgO (100), SLs with a bilayer period larger than 2.5 nm show a strong reflection at  $2\theta \sim 44^\circ$ . This is pictured in Fig. 2c for a SL with  $\Lambda = 4.0$  nm and might be due the sizeable lattice mismatch between TiN and  $\text{Cr}_{0.37}\text{Al}_{0.63}\text{N}$  layers and their near epitaxial SL structure leading to separate 0<sup>th</sup> order (200) peaks. Consequently, individual sequences of satellite peaks arise, as suggested by Fig. 2c, underlining the high epitaxial quality. The separate 0<sup>th</sup> order and individual sequences of satellite peaks are not often observed, as typically SL films (for, e.g., semiconductors) are developed with layers having a small lattice mismatch. Alternatively, the strong reflection at  $2\theta \sim 44^\circ$  could also be the sole 0<sup>th</sup> order SL (200) peak shifting to a significantly larger diffraction angle. The (200) MgO double peak, caused by the radiation doublet of Cu

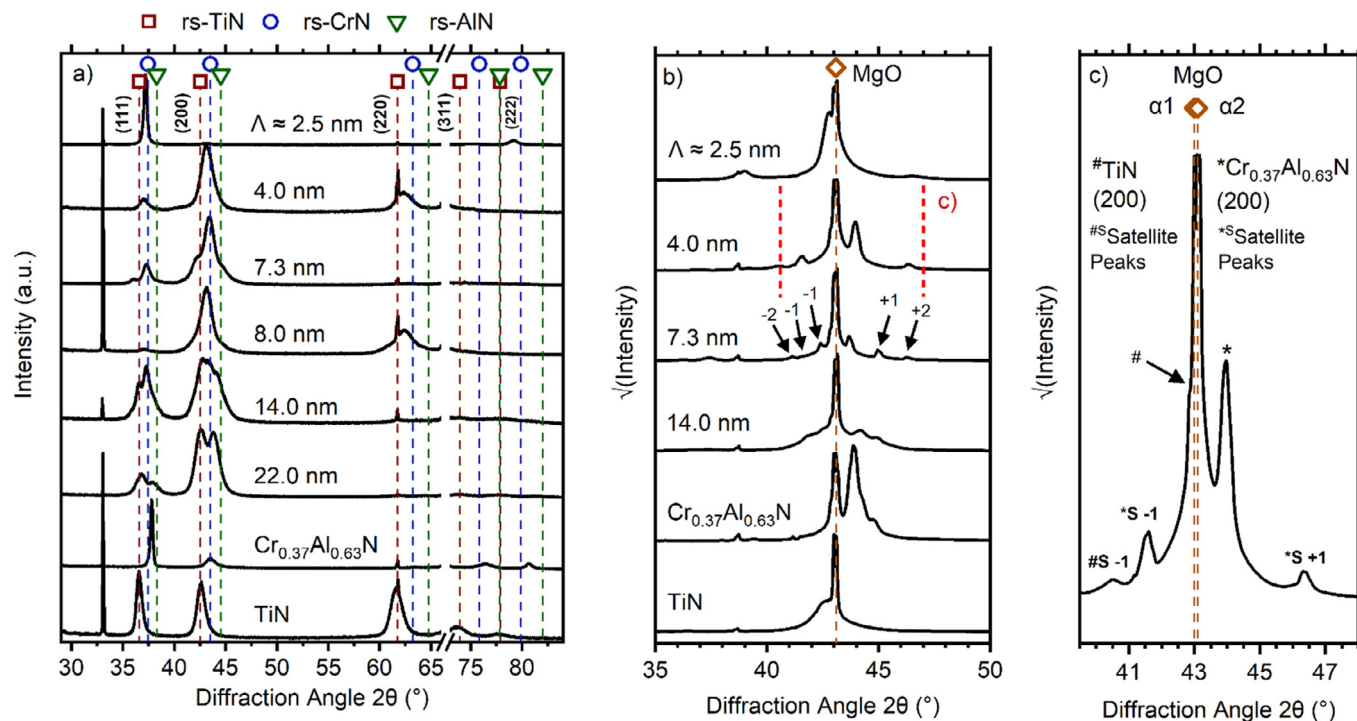


**Fig. 2.** XRD patterns of TiN/Cr<sub>0.37</sub>Al<sub>0.63</sub>N superlattices and monolithically grown TiN and Cr<sub>0.37</sub>Al<sub>0.63</sub>N on Si (100) (a), and MgO (100) (b) substrates. (a) features diffraction patterns of all superlattices, whereas (b) only shows selected ones, with satellite peaks exemplified by arrows for the SL with  $\Lambda = 7.3$  nm. The plot in (c) provides a detailed view of the (200) peak of a TiN/Cr<sub>0.37</sub>Al<sub>0.63</sub>N superlattice with a bilayer period of 4.0 nm. Satellite peaks in (b) and (c) are marked according to their position in relation to their corresponding 0<sup>th</sup> order peak (+, -) and their order (1, 2).

$K\alpha_1$  and Cu  $K\alpha_2$ , is also pictured in Fig. 2c. For a thorough investigation and verification of the satellite peaks, more sophisticated modelling procedures, such as the approach of Fullerton et al. [74], might be employed to fit the SL XRD patterns.

### 3.2.2. Transmission electron microscopy

Detailed TEM investigations confirm the well-defined nanolayered architecture of our TiN/Cr<sub>0.37</sub>Al<sub>0.63</sub>N SLs, as demonstrated by the examples with bilayer periods of 2.5 and 7.3 nm presented in Fig. 3. The films on Si (100) (Figs. 3a and b) show a distinct columnar growth structure, characteristic for a more random growth orientation, which is proven by SAED (see the small insets in Fig. 3a and b). However, within the columns, the layers do grow coherently, as indicated by the similar TEM contrast spanning across several layers. The TEM micrographs in Figs. 3c and d show that using MgO (100) as a substrate leads to a significantly enhanced epitaxial growth; individual columns are virtually unrecognisable. The corresponding SAED investigation (small inset in Fig. 3c) confirms the almost single-crystalline microstructure of the SL with a bilayer period of 2.5 nm on MgO across the entire coating thickness. Contrastingly, for the  $\Lambda = 7.3$  nm SL, nearly perfect epitaxy on MgO (100) is only present for the initial ~200 nm, after which the growth mode changes to more columnar polycrystalline, but still highly 100-oriented (see inset of Fig. 3d). The HRTEM investigations of these two SLs on MgO (Fig. 3e and f) – taken from fully epitaxial regions – confirm the high quality and bilayer periods of 2.5 and 7.3 nm, respectively.

These high-quality SLs are further investigated by HRTEM to study their dislocation densities, which are averaged from three different regions. The areal dislocation density of  $(2.4 \pm 0.6) \cdot 10^{12}$  cm<sup>-2</sup> for the SL with  $\Lambda = 2.5$  nm is markedly lower than the  $(4.7 \pm 0.9) \cdot 10^{12}$  cm<sup>-2</sup> for the SL with  $\Lambda = 7.3$  nm. Exemplifying HRTEM micrographs are provided in Figs. 4a and b. Please consider that these HRTEM investigations are unable to distinguish between misfit and growth-induced dislocations. However, the latter are essen-

tially identical in both superlattices, since their deposition conditions are identical. Thus, we conclude that the density of misfit dislocations increases with increasing bilayer period, through which coherency strains are relieved.

### 3.3. Indentation modulus & hardness

In excellent agreement with DFT predictions, the indentation moduli (Fig. 5) of polycrystalline TiN and Cr<sub>0.37</sub>Al<sub>0.63</sub>N – as a result of the growth on Si (100) – are essentially identical with  $368.3 \pm 5.5$  and  $363 \pm 4.2$  GPa, respectively. The indentation moduli of polycrystalline TiN/Cr<sub>0.37</sub>Al<sub>0.63</sub>N superlattices roughly follow the rule of mixture, fluctuating around these values between  $358.6 \pm 5.6$  GPa for  $\Lambda = 7.3$  nm and  $382.8 \pm 5.3$  GPa for  $\Lambda = 22.0$  nm.

On MgO (100) substrates, the TiN and Cr<sub>0.37</sub>Al<sub>0.63</sub>N films are highly 100-oriented and essentially single-crystalline (as discussed above, and shown in Figs. 2b, 3c and d). Their indentation moduli of  $497.3 \pm 3.9$  GPa and  $469.2 \pm 10.6$  GPa, respectively, show a sizeable difference. In agreement with our experiments, DFT calculations also suggest a higher  $E_{100}$  for TiN (527 GPa [58]) than for Cr<sub>0.37</sub>Al<sub>0.63</sub>N.  $E_{100}$  is 406 GPa for Cr<sub>0.44</sub>Al<sub>0.56</sub>N, as obtained from elastic constants reported in [52]. TiN is a highly anisotropic material, for which  $E_{100} > E_{110} > E_{111}$  holds true [58,75]. Thus, it is plausible that the highly 100-oriented film on MgO (100) gives a higher modulus than the more randomly oriented film on Si (100). In contrast to that, Cr<sub>0.37</sub>Al<sub>0.63</sub>N is close to the chemical composition window ( $x = 0.44$ – $0.56$  [52]) of Cr<sub>1-x</sub>Al<sub>x</sub>N, which promises elastic isotropy. The DFT data suggest that a reverse order of the directional Young's moduli of  $E_{111} > E_{110} > E_{100}$  applies for Cr<sub>0.37</sub>Al<sub>0.63</sub>N. Thus, our experiments with a lower indentation modulus for the 111-oriented film on Si (100) compared to the 100-oriented film on MgO (100), can only be explained by differences in their residual stresses and grain size. The smaller the grain size (the larger the grain boundary fraction) or the smaller the compressive stress state (the larger the tensile stress state) the smaller

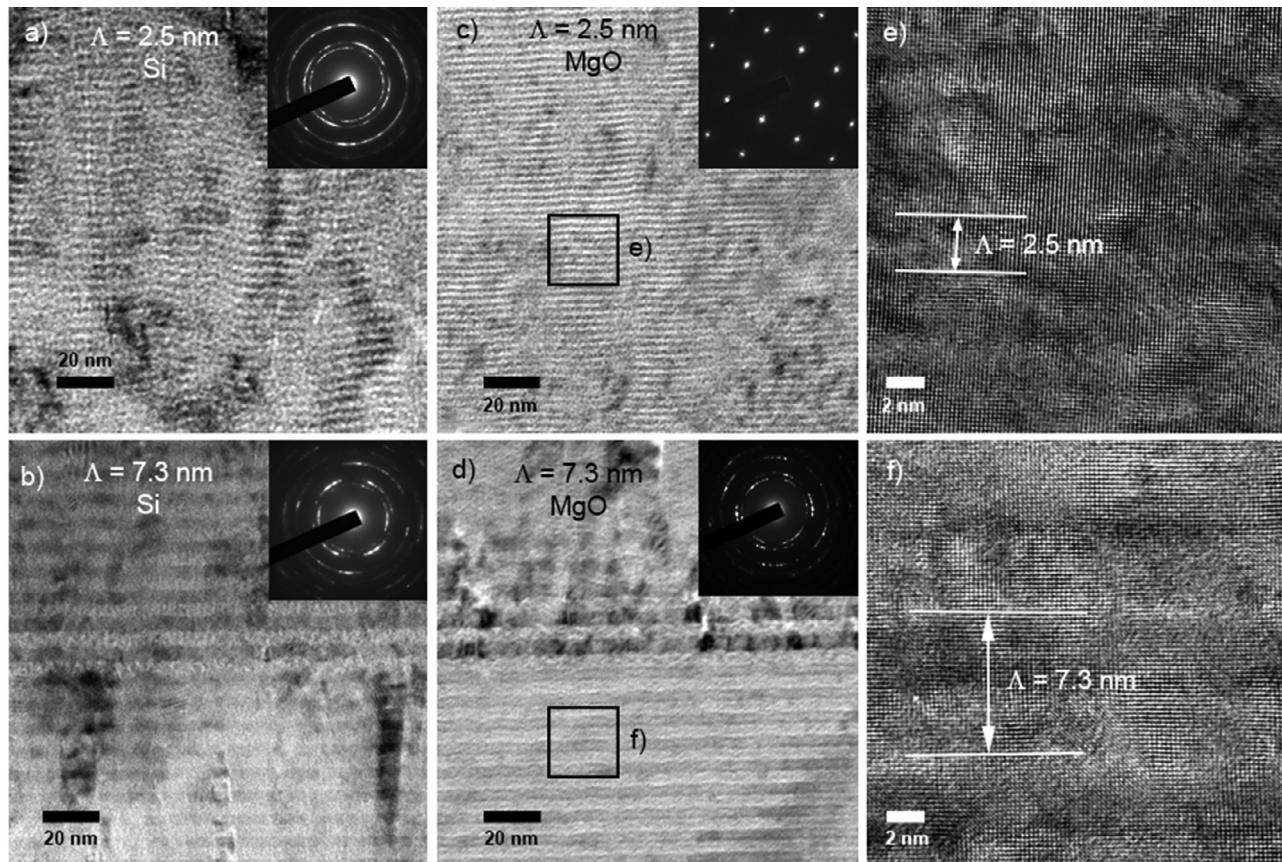


**Fig. 3.** Cross-sectional bright field TEM micrographs of TiN/Cr<sub>0.37</sub>Al<sub>0.63</sub>N SLs with bilayer periods of 2.5 nm (a) and 7.3 nm (b) deposited on Si (100), as well as 2.5 nm (c) and 7.3 nm (d) grown on MgO (100). SAED patterns are inserted into the top right corner of the corresponding micrographs. (e) and (f), are HRTEM images of SLs with  $\Lambda = 2.5$  and 7.3 nm, taken from fully epitaxial regions indicated in (c) and (d), respectively.

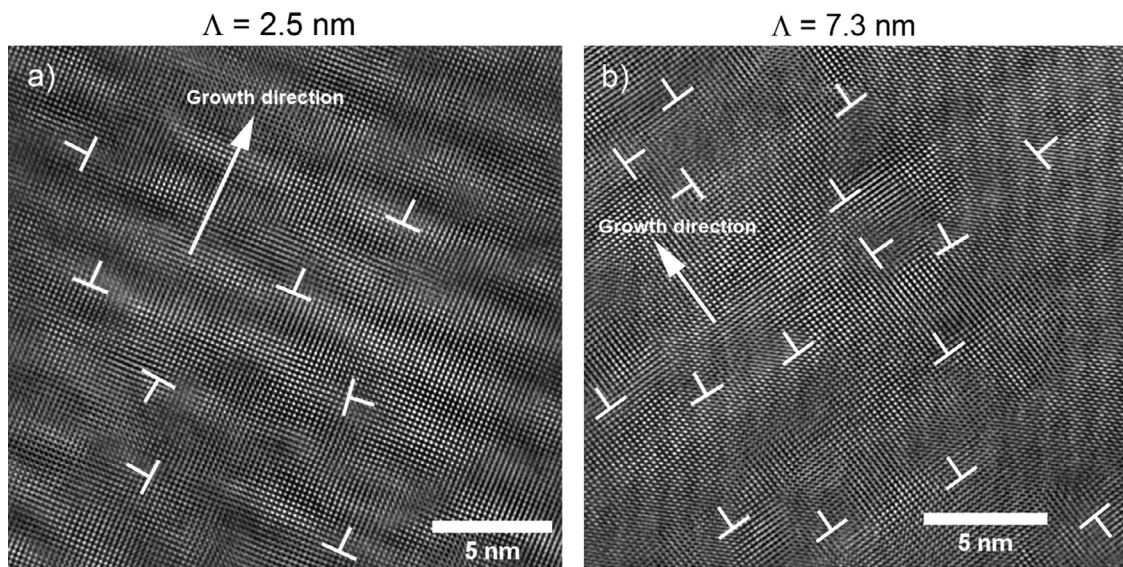


**Fig. 4.** HRTEM micrographs of TiN/Cr<sub>0.37</sub>Al<sub>0.63</sub>N SLs with bilayer periods of 2.5 nm (a), and 7.3 nm (b) deposited on MgO (100) substrates. Dislocations are highlighted in both images. Please note that these images are Wiener filtered. The viewing axis is the [100] direction.

the elastic modulus [76–79]. This fits to our data, as the films on Si (100) have a smaller grain size than those on MgO (100). Additionally, we also showed in an earlier study [80] that for films thinner than 8  $\mu\text{m}$  the substrate matters (stiffer substrates lead to higher indentation moduli). In agreement with the observations for the SL films on Si (100), also those on MgO (100) show no clear bilayer-period-dependent trend, following the rule of mixture.

Similar to the indentation moduli, the films grown on MgO (100) outperform those grown on Si (100) also in terms of hardness. But contrary to the indentation modulus, the superlattice films are harder than their constituents, at least for  $\Lambda = 4.0$ , 7.3, and 8.0 nm, regardless if grown on Si (100) or MgO (100) (Fig. 6). The softest superlattice films are those with the smallest bilayer period of 2.5 nm; a typically observed behaviour for TMNs, due to

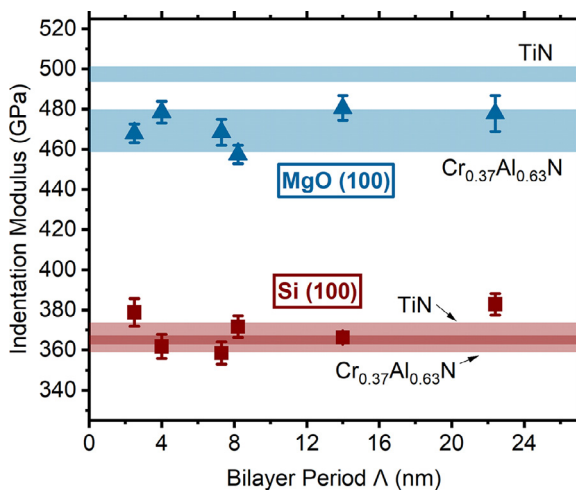


**Fig. 5.** Indentation modulus of TiN/Cr<sub>0.37</sub>Al<sub>0.63</sub>N as a function of the bilayer period on Si (100) and MgO (100) substrates. The indentation moduli of TiN and Cr<sub>0.37</sub>Al<sub>0.63</sub>N [also on Si (100) and MgO (100)] are indicated with horizontal bars; their widths represent the measurement error. On Si (100) substrates, the indentation moduli of TiN and Cr<sub>0.37</sub>Al<sub>0.63</sub>N overlap, due to the polycrystalline character of the films, in agreement with DFT-based calculations (Fig. 1).

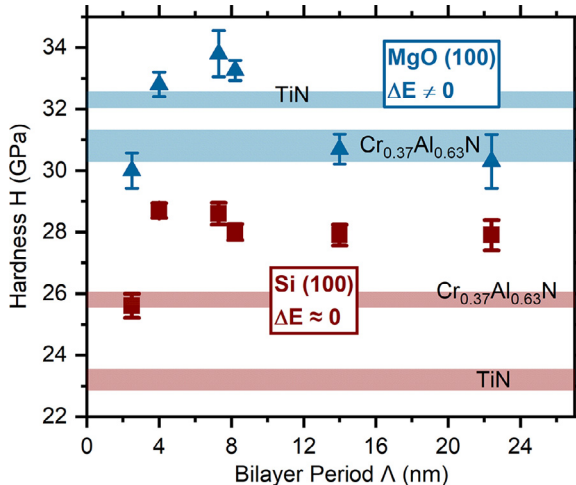


**Fig. 6.** Juxtaposition of the bilayer-period-dependent hardness trends of TiN/(Cr,Al)N superlattices on Si (100), and MgO (100) substrates. The values of monolithic TiN, and (Cr,Al)N are provided as reference in the shape of horizontal bars, the thicknesses of which represent the corresponding measurement error.

the limited interface sharpness and reduced barrier against dislocation glide for small bilayer periods. The hardest SL films on Si (100) are those with  $\Lambda = 4.0$  and 7.3 nm, having  $H = 28.7 \pm 0.2$  and  $28.6 \pm 0.4$  GPa, respectively. These are excelled by  $\sim 5$  GPa by the SL film on MgO (100) with a bilayer period of 7.3 nm, having  $H = 33.8 \pm 0.8$  GPa. Overall, the hardness of the SL films grown on Si (100) shows only a small dependence on the bilayer period, for  $\Lambda > 2.5$  nm. But when growing the films on MgO (100), they share more similarities with previous reports on the superlattice effect, such as TiN/VN [31], TiN/(V,Nb)N [32,81], TiN/CrN [25], and TiN/WN [30]. Still, these systems provide a more pronounced hardness peak than our TiN/Cr<sub>0.37</sub>Al<sub>0.63</sub>N system – even when grown on MgO (100). An explanation for this behaviour (nearly no bilayer-period-dependent superlattice effect for our films on Si (100) and only a smaller effect for our films on MgO (100) than in the reported systems listed above) rests on the shear moduli difference of the involved materials.

More random oriented and polycrystalline TiN and Cr<sub>0.37</sub>Al<sub>0.63</sub>N – as present on Si (100) – have similar shear moduli, and there-

fore exhibit almost no bilayer-period-dependent superlattice effect. If grown nearly single-crystalline and with a pronounced 100-orientation – as present on MgO (100) – the indentation moduli and hence the shear moduli are sizeably different. This difference is still not as pronounced as for the mentioned systems above, and therefore also the superlattice effect is not as pronounced. Consequently, the lattice mismatch alone (as in our system) is insufficient for obtaining a bilayer-period-dependent superlattice effect. Elastic differences between the layers, contrastingly, are crucial in that regard. This aligns well with studies of Chu and Barnett [33], as well as Barnett and Madan [82], who have identified shear moduli differences of the involved materials as the main contributing factor to the so-called hardness-related superlattice effect in TMN thin films.

### 3.4. Fracture toughness

**Fig. 7a** depicts raw load-deflection data of all tested microcantilevers of TiN, Cr<sub>0.37</sub>Al<sub>0.63</sub>N, and the SLs with  $\Lambda = 2.5$ , 7.3, and 14.0 nm. Representative load-deflection curves of each sample, normalised in terms of stress intensity and bending strain, are presented in **Fig. 7b**. The conversion of the deflection into bending strain for notched cantilevers in particular entails an array of inaccuracies. Firstly, the simple conversion does not account for stress/strain concentrations at the notch tip, providing a source of underestimation. Secondly, we took the thickness of the coating below the notch (hence, the thickness of the cantilever  $w$  minus the notch depth  $c_0$ ) as the thickness of the cantilever cross-section, which may also introduce a degree of inaccuracy. Thus, the absolute values presented in **Fig. 7** should be taken with care, especially when comparing them to values recorded for unnotched beams. The normalised curves show that the presented cantilevers of TiN, Cr<sub>0.37</sub>Al<sub>0.63</sub>N, and the SL with a bilayer period of 14.0 nm match very closely in terms of stiffness. The superlattices with bilayer periods of 7.3 and 2.5 nm deviate slightly from this alignment. However, both divergences are relatively small, and neither is also sufficiently captured by the measurements of the indentation modulus in the previous section, thus leading us to conclude that they can be attributed to measurement errors of – most likely – the cantilever geometries.

Overall, the normalised curves show that the SLs exceed monolithic TiN and Cr<sub>0.37</sub>Al<sub>0.63</sub>N in terms of critical stress intensity, elastic deformability, and fracture energy (which – in this case – would be roughly proportional to the area under the normalised curves). All three quantities contribute towards the overall toughness of the material in question. Comparing SLs with different bilayer periods with each other, however, shows that samples which perform better in terms of one of these properties, exhibit a slight deficiency in the other two. Therefore, this analysis does not clearly identify a bilayer period that outperforms the others in toughness-related characteristics.

Looking at the elastic bendability specifically, the lattice mismatch between the involved layers in the superlattice architecture also seems to enhance the maximum achievable bending strain of the SL films compared to the monolithic compounds. **Fig. 7b** shows that the SLs reach a maximum bending strain of approximately 1.47 % with  $\Lambda = 2.5$  nm, favourably exceeding the 1.18 and 0.81 % for TiN and Cr<sub>0.37</sub>Al<sub>0.63</sub>N, respectively. Investigations of (Al,Ta,Ti,V,Zr)N high-entropy nitride thin films, produced, measured, and evaluated using the same methods as the current study yield bending strain values of 1.56 and 1.17 % with and without Si alloying, respectively [16].

**Fig. 7** suggests that the fracture toughness trends of the present study are not the result of irregularities in the crack propagation, since neither the raw nor the normalised load-deflection curves in **Fig. 7** depict any such irregularities. However, given the small

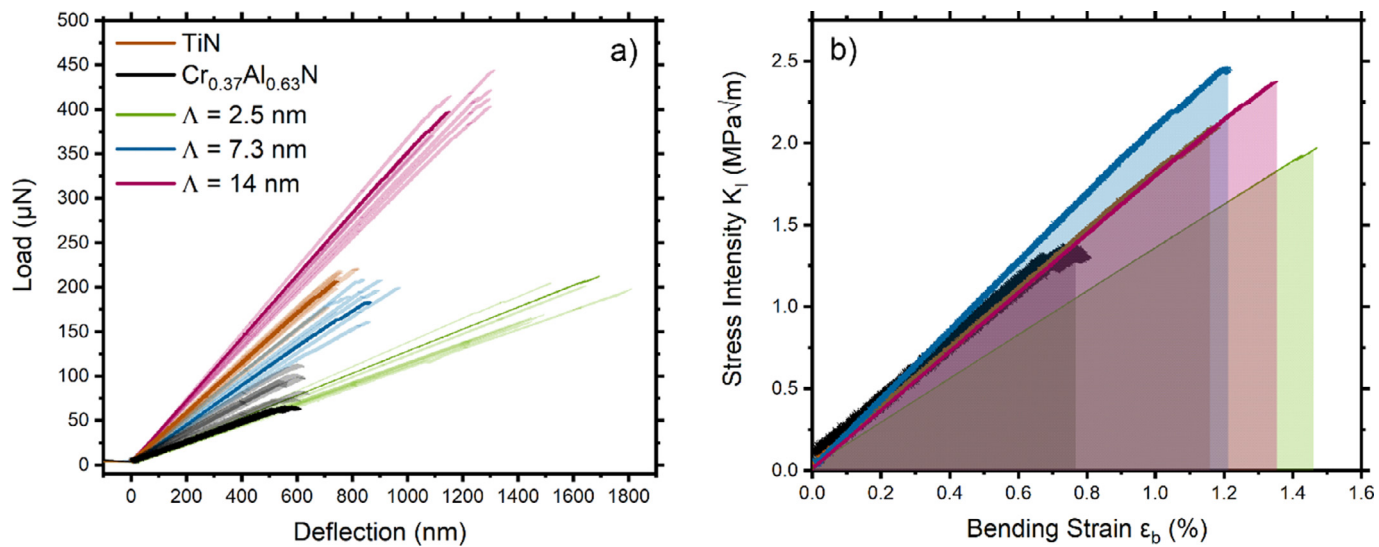
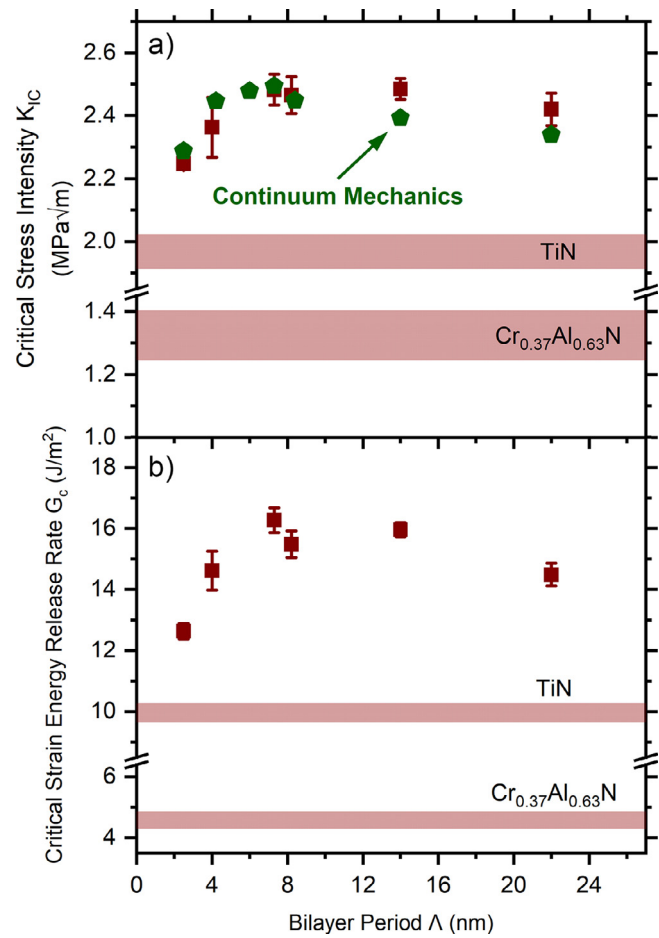


**Fig. 7.** Load-deflection data (a) of all cantilevers of monolithic TiN, and Cr<sub>0.37</sub>Al<sub>0.63</sub>N, as well as of three selected TiN/Cr<sub>0.37</sub>Al<sub>0.63</sub>N superlattices. Representative cantilevers are depicted opaquely in (a), and in a normalised plot – in terms of stress intensity and bending strain – in (b).

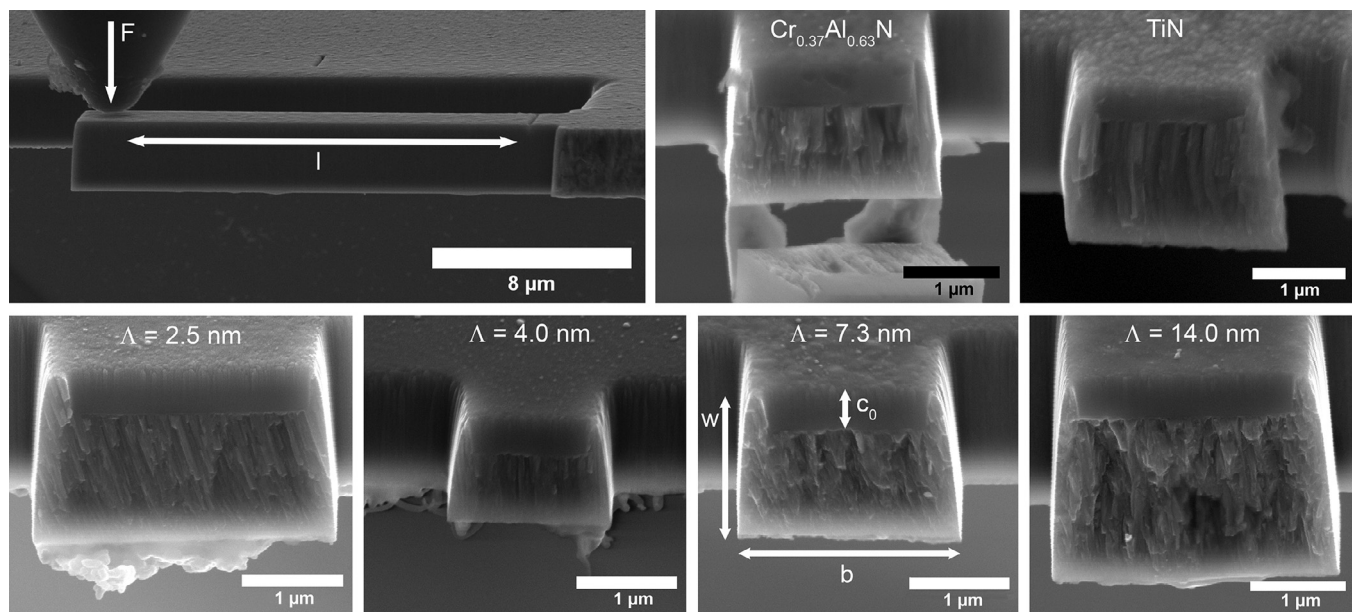
length scale of the SL architecture, such events could not be resolved by the nanomechanical testing system, even if they did occur.

Fig. 8 shows the critical stress intensity K<sub>IC</sub> and critical strain energy release rate G<sub>C</sub> of our SL and monolithic coatings grown on Si (100), respectively. Due to its relation to K<sub>IC</sub> (Fig. 8a), the trend in G<sub>C</sub> (Fig. 8b) effectively reflects an accentuated version of the fracture toughness (K<sub>IC</sub>) trend. Despite the near absence of elastic differences between the layers, our SL films consistently allow for higher K<sub>IC</sub> and G<sub>C</sub> values than their constituent compounds TiN and Cr<sub>0.37</sub>Al<sub>0.63</sub>N. Apart from a small decrease at lower bilayer periods, K<sub>IC</sub> and G<sub>C</sub> depend only weakly on the bilayer period. Thus, in context with preceding studies on TMN SLs [25][30], our current investigations suggest that a sizeable lattice mismatch (as present for TiN and Cr<sub>0.37</sub>Al<sub>0.63</sub>N) between the involved layers is sufficient to induce a superlattice effect and elevate the fracture toughness (and hardness) of TMN SLs beyond the values of their constituent materials. But for a strong bilayer-period-dependent behaviour, and to maximise the extent of the toughness enhancement, elastic differences between the layers are needed. The TiN/CrN system – featuring moderate elastic and structural mismatches between the involved materials – shows a noticeable dependence of the fracture toughness on the bilayer period [25]. Strongly 100-oriented and quasi-monocrystalline TiN/WN SLs – composed of layer materials with significantly different elastic properties and almost identical lattice parameters – exhibit a pronounced enhancement in fracture toughness compared to the constituent components, as well as a strong dependence on the bilayer period [30].

For an improved understanding of the involved mechanisms, we contrast the experimentally produced K<sub>IC</sub> values with modelled ones. As outlined in the methodology section, the analytical continuum-mechanics-based model implements experimentally measured intrinsic fracture toughness values (2.0±0.1 MPa $\sqrt{m}$  for TiN, and 1.3±0.1 MPa $\sqrt{m}$  for Cr<sub>0.37</sub>Al<sub>0.63</sub>N) and the stiffness tensor components (taken from [58] and [52]) of the monolithic materials. Thereby, it predominantly focuses on coherency strains and misfit dislocations, caused by lattice mismatch of the layers. Based on TEM and X-ray reflectivity investigations on polycrystalline TiN/CrN SLs [25], we set the interface width to 0.8 nm for all our SLs. The model predicts that for the two lowest bilayer periods dislocations form in the first Cr<sub>0.37</sub>Al<sub>0.63</sub>N layer only, while the rest of the film grows coherently. This results in a rearrangement of misfit



**Fig. 8.** Critical stress intensity K<sub>IC</sub> (a) and critical strain energy release rate G<sub>C</sub> (b) as a function of the bilayer period Λ for our TiN/Cr<sub>0.37</sub>Al<sub>0.63</sub>N SLs from which the Si (100) substrate material was removed. Corresponding values for monolithic TiN (K<sub>IC</sub> = 2.0±0.1 MPa $\sqrt{m}$  and G<sub>C</sub> = 10±0.3 J/m<sup>2</sup>) and Cr<sub>0.37</sub>Al<sub>0.63</sub>N (K<sub>IC</sub> = 1.3±0.1 MPa $\sqrt{m}$  and G<sub>C</sub> = 4.6±0.3 J/m<sup>2</sup>) are indicated with horizontal bars. Pentagonal data points reflect the outcome of the continuum mechanical calculations.



**Fig. 9.** The top left image depicts a scanning electron microscopy (SEM) micrograph of a typical microcantilever before testing (including the spherical indenter tip). The remaining images show SEM micrographs of representative fracture cross-sections of monolithic TiN, and  $(\text{Cr}, \text{Al})\text{N}$ , as well as  $\text{TiN}/(\text{Cr}, \text{Al})\text{N}$  superlattices with 4 different bilayer periods (2.5 nm, 4.0 nm, 7.3 nm, and 14 nm).

stresses throughout the superlattice, but the strain energy stored in the film stays virtually constant with respect to  $\Lambda$ . Hence, removing the substrate leads to a stress profile similar to that of a dislocation-free system. The weak toughness enhancement with increasing  $\Lambda$  (at low  $\Lambda$ ) is thus mostly reflective of the increase in layer thickness – amplifying the toughening effect of compressive stresses. Only once a certain critical bilayer period is exceeded ( $\Lambda_{\text{crit}} \approx 4.8$  nm) and misfit dislocations form in all layers, the strain energy within the system is gradually reduced. Due to the ensuing reduction of coherency strains,  $K_{\text{IC}}$  decreases slightly and levels out at higher bilayer periods. Thus, the fracture toughness values recorded for the present  $\text{TiN}/\text{Cr}_{0.37}\text{Al}_{0.63}\text{N}$  SL system do not – strictly speaking – represent the intrinsic material property, but rather a function of the coherency-induced stress profile across the film. It should also be noted that if misfit dislocation formation was not considered in the model, the stress state within the layers would remain constant with respect to  $\Lambda$  and a continuous increase of  $K_{\text{IC}}$  with the layer thicknesses (i.e.  $\Lambda$ ) would be observed – according to the employed weight function [66].

For the specific fully brittle SL system of the present study – consisting of layers with closely matching elastic and mechanical properties – the outlined analytical model provides reliable values and a potential explanation for the observed toughness trend. It has to be taken into consideration, however, that the methodology may not be applicable to other SL systems. Heightened differences in the structural and mechanical properties between the SL layers may potentially introduce features – such as completely incoherent interfaces, irregularities in the crack propagation (e.g. deflection, trapping), yielding of one or both of the layer materials, or stress states that differ significantly from our system – which are not accounted for by the analytical model [55].

The juxtaposition of SEM fracture cross-sections of TiN,  $\text{Cr}_{0.37}\text{Al}_{0.63}\text{N}$ , and the SLs with  $\Lambda = 2.5, 4.0, 7.3$ , and 14.0 nm, Fig. 9, shows a slightly coarser columnar grain structure for TiN and  $\text{Cr}_{0.37}\text{Al}_{0.63}\text{N}$  – compared to the SLs. This agrees with our XRD investigations, indicating also coarser coherently diffracting domain sizes especially for  $\text{Cr}_{0.37}\text{Al}_{0.63}\text{N}$ . In general, the microstructure and grain size has a profound impact on fracture toughness [83,84], explaining the strikingly low values for  $\text{Cr}_{0.37}\text{Al}_{0.63}\text{N}$ . At

this point, it should be noted that our analytical model uses the experimentally measured fracture toughness and indentation moduli of the monolithic materials as input. Thus, the model implicitly assumes that the grain structure in the SL films is the same as in the monolithic films and still predicts an improved fracture toughness for the  $\text{TiN}/\text{Cr}_{0.37}\text{Al}_{0.63}\text{N}$  superlattices. Hence, we envision that (for the SLs) the small offset between the fracture toughness values of the analytical model and those of the bending tests (especially at higher  $\Lambda$ ) may be partially caused by the difference in grain size between the monolithic coatings and the superlattices.

Fig. 9 also demonstrates that the thickness of our coatings ranged from 1.5  $\mu\text{m}$  to 2.8  $\mu\text{m}$  and that the  $c_0/w$  ratios of our cantilevers are all relatively similar. Also, the  $c_0/w$  (notch depth to thickness) ratios of the cantilevers varied roughly only between 0.21 and 0.33. According to the findings of Iqbal et al. [85] and Brinckmann et al. [9], our cantilever geometries should therefore provide results of reasonable accuracy. Still, comparisons of the absolute fracture toughness values of different studies determined via microcantilever approaches [8,49] should always be treated with care, due to the geometry-sensitive nature of the method [9,86,87].

#### 4. Summary and conclusions

Consulting pre-existing DFT-based data, we designed  $\text{TiN}/\text{Cr}_{0.37}\text{Al}_{0.63}\text{N}$  superlattices (SLs), in which the differences in the polycrystalline elastic moduli between the layers are eliminated. This allowed us to analyse specifically the effect of the lattice mismatch between the involved materials on the toughness-enhancing superlattice effect in transition metal nitride (TMN) thin films.

All our films crystallised in the cubic rock-salt structure, with films deposited on Si (100) substrates providing polycrystalline samples and MgO (100) substrates producing strongly (100)-oriented coatings. Our nanoindentation results revealed virtually identical indentation moduli for the polycrystalline samples of monolithic TiN and  $\text{Cr}_{0.37}\text{Al}_{0.63}\text{N}$  on Si (100). On MgO (100), the monolithic films showed a slight disparity in terms of their indentation moduli. The indentation moduli of all  $\text{TiN}/\text{Cr}_{0.37}\text{Al}_{0.63}\text{N}$  SLs on both substrate types consistently lay in between the constituent

materials – independent of the bilayer period ( $\Lambda$ ). The hardness of the polycrystalline TiN/Cr<sub>0.37</sub>Al<sub>0.63</sub>N SLs was enhanced slightly beyond monolithic TiN (23.2±0.4 GPa), and Cr<sub>0.37</sub>Al<sub>0.63</sub>N (25.8±0.3 GPa) up to 28.7±0.2 GPa, mostly independent of the bilayer period. Contrastingly, the (100)-oriented SLs showed a bilayer-period-dependent hardness enhancement, with a maximum of 33.8±0.8 GPa at bilayer period of 7.3 nm.

The SL architecture also raised the fracture toughness  $K_{IC}$  of TiN/Cr<sub>0.37</sub>Al<sub>0.63</sub>N (2.5±0.1 MPa $\sqrt{m}$  at  $\Lambda = 7.3$  nm) above that of monolithic TiN (2±0.1 MPa $\sqrt{m}$ ) and Cr<sub>0.37</sub>Al<sub>0.63</sub>N (1.3±0.1 MPa $\sqrt{m}$ ) for all bilayer periods. Apart from a small decrease at lower bilayer periods, we did not record a measurable dependence of the fracture toughness on the bilayer period. We used an analytical continuum-mechanics-based model to calculate the theoretical fracture toughness of TiN/Cr<sub>0.37</sub>Al<sub>0.63</sub>N SLs based on the evolution of coherency strains and misfit dislocations with changing bilayer period. Superimposition of experimental and calculational data demonstrated that initiation of misfit dislocation formation with increasing  $\Lambda$  – and the associated change of coherency strains – in the involved layer materials is governing the toughness enhancement in TiN/Cr<sub>0.37</sub>Al<sub>0.63</sub>N SLs. In a broader context, the findings of the present study suggest that both the lattice and elastic mismatch contribute towards the toughness-enhancing SL effect in TMNs. Thereby, the lattice mismatch elevates the fracture toughness of SLs above that of the monolithic materials (largely independent of  $\Lambda$ ), while elastic differences cause a strong bilayer period dependence – further maximising the fracture toughness.

## Declaration of Competing Interest

The authors declare that they have no known competing financial interests or personal relationships that could have appeared to influence the work reported in this paper

## Acknowledgement

JB, AW, DH, PHM, and MB highly acknowledge the financial support of the Austrian Science Fund (FWF): P30341-N36. The authors acknowledge the use of the facilities of USTEM and XRC at TU Wien. We thank the Institute for Mechanics of Materials and Structures (TU Wien) for providing the PicoIndenter PI-85.

## Supplementary materials

Supplementary material associated with this article can be found, in the online version, at doi:10.1016/j.actamat.2020.10.068.

## References

- [1] I. Milošev, H.-H. Strehblow, B. Navinšek, Comparison of TiN, ZrN and CrN hard nitride coatings: Electrochemical and thermal oxidation, *Thin Solid Films* 303 (1997) 246–254, doi:10.1016/S0040-6090(97)00069-2.
- [2] B. Navinšek, S. Seal, Transition metal nitride functional coatings, *JOM* 53 (2001) 51–54, doi:10.1007/s11837-001-0072-1.
- [3] S. Veprek, The search for novel, superhard materials, *J. Vac. Sci. Technol. A Vacuum, Surfaces, Film* 17 (1999) 2401–2420, doi:10.1116/1.581977.
- [4] S. Veprek, M.J.G. Veprek-Heijman, Industrial applications of superhard nanocomposite coatings, *Surf. Coatings Technol.* 202 (2008) 5063–5073, doi:10.1016/j.surfcoat.2008.05.038.
- [5] D. Rafaja, C. Wüstefeld, M. Motylenko, C. Schimpf, T. Barsukova, M.R. Schwarz, E. Kroke, Interface phenomena in (super)hard nitride nanocomposites: from coatings to bulk materials, *Chem. Soc. Rev.* 41 (2012) 5081, doi:10.1039/c2cs15351c.
- [6] M. Sebastiani, K.E. Johanns, E.G. Herbert, F. Carassiti, G.M. Pharr, A novel pillar indentation splitting test for measuring fracture toughness of thin ceramic coatings, *Philos. Mag.* 95 (2015) 1928–1944, doi:10.1080/14786435.2014.913110.
- [7] K. Matoy, T. Detzel, M. Müller, C. Motz, G. Dehm, Interface fracture properties of thin films studied by using the micro-cantilever deflection technique, *Surf. Coatings Technol.* 204 (2009) 878–881, doi:10.1016/j.surfcoat.2009.09.013.
- [8] K. Matoy, H. Schönher, T. Detzel, T. Schöberl, R. Pippan, C. Motz, G. Dehm, A comparative micro-cantilever study of the mechanical behavior of silicon based passivation films, *Thin Solid Films* 518 (2009) 247–256, doi:10.1016/j.ts.2009.07.143.
- [9] S. Brinckmann, K. Matoy, C. Kirchlechner, G. Dehm, On the influence of micro-cantilever pre-crack geometries on the apparent fracture toughness of brittle materials, *Acta Mater.* 136 (2017) 281–287, doi:10.1016/j.actamat.2017.07.014.
- [10] H. Kindlund, D.G. Sangiovanni, I. Petrov, J.E. Greene, L. Hultman, A review of the intrinsic ductility and toughness of hard transition-metal nitride alloy thin films, *Thin Solid Films* 688 (2019) 137479, doi:10.1016/j.ts.2019.137479.
- [11] M. Bartosik, C. Rumeau, R. Hahn, Z.L. Zhang, P.H. Mayrhofer, Fracture toughness and structural changes in the TiAlN system upon annealing, *Sci. Rep.* 7 (2017) 16476, doi:10.1038/s41598-017-16751-1.
- [12] K. Yalamanchili, I.C. Schramm, E. Jiménez-Piqué, L. Rogström, F. Mücklich, M. Odén, N. Ghafoor, Tuning hardness and fracture resistance of ZrN/Zr0.63Al0.37N nanoscale multilayers by stress-induced transformation toughening, *Acta Mater.* 89 (2015) 22–31, doi:10.1016/j.actamat.2015.01.066.
- [13] M. Bartosik, R. Hahn, Z.L. Zhang, I. Ivanov, M. Arndt, P. Polcik, P.H. Mayrhofer, Fracture toughness of Ti-Si-N thin films, *Int. J. Refract. Met. Hard Mater.* 72 (2018) 78–82, doi:10.1016/j.jrmhm.2017.12.015.
- [14] M. Sperr, Z.L. Zhang, Y.P. Ivanov, P.H. Mayrhofer, M. Bartosik, Correlating elemental distribution with mechanical properties of TiN/SiNx nanocomposite coatings, *Scr. Mater.* 170 (2019) 20–23, doi:10.1016/j.scriptamat.2019.05.020.
- [15] R. Daniel, M. Meindlhuber, W. Baumegger, J. Todt, J. Zalesak, T. Ziegelwanger, C. Mitterer, J. Keckes, Anisotropy of fracture toughness in nanostructured ceramics controlled by grain boundary design, *Mater. Des.* 161 (2019) 80–85, doi:10.1016/j.matdes.2018.11.028.
- [16] R. Hahn, A. Kirnbauer, M. Bartosik, S. Kolozsvári, P.H. Mayrhofer, Toughness of Si alloyed high-entropy nitride coatings, *Mater. Lett.* 251 (2019) 238–240, doi:10.1016/j.matlet.2019.05.074.
- [17] H. Kindlund, D.G. Sangiovanni, L. Martínez-de-Olcoz, J. Lu, J. Jensen, J. Birch, I. Petrov, J.E. Greene, V. Chirita, L. Hultman, Toughness enhancement in hard ceramic thin films by alloy design, *APL Mater.* 1 (2013) 042104, doi:10.1063/1.4822440.
- [18] H. Kindlund, D.G. Sangiovanni, J. Lu, J. Jensen, V. Chirita, J. Birch, I. Petrov, J.E. Greene, L. Hultman, Vacancy-induced toughening in hard single-crystal V0.5Mo0.5Nx/MgO(0 0 1) thin films, *Acta Mater.* 77 (2014) 394–400, doi:10.1016/j.actamat.2014.06.025.
- [19] H. Kindlund, D.G. Sangiovanni, J. Lu, J. Jensen, V. Chirita, I. Petrov, J.E. Greene, L. Hultman, Effect of WN content on toughness enhancement in V<sub>1-x</sub>W<sub>x</sub>N/MgO(001) thin films, *J. Vac. Sci. Technol. A Vacuum, Surfaces, Film* 32 (2014) 030603, doi:10.1116/1.4867610.
- [20] W.M. Seidl, M. Bartosik, S. Kolozsvári, H. Bolvardi, P.H. Mayrhofer, Influence of Ta on the fracture toughness of arc evaporated Ti-Al-N, *Vacuum* 150 (2018) 24–28, doi:10.1016/j.vacuum.2018.01.028.
- [21] T. Glechner, R. Hahn, T. Wójcik, D. Holec, S. Kolozsvári, H. Zaid, S. Kodambaka, P.H. Mayrhofer, H. Riedl, Assessment of ductile character in superhard Ta-C-N thin films, *Acta Mater.* 179 (2019) 17–25, doi:10.1016/j.actamat.2019.08.015.
- [22] P. Dubey, S. Srivastava, R. Chandra, C.V. Ramana, Toughness enhancement in zirconium-tungsten-nitride nanocrystalline hard coatings, *AIPI Adv.* 6 (2016) 075211, doi:10.1063/1.4959224.
- [23] M.P. Manoharan, A. Desai, A. Haque, Fracture Toughness of Titanium - Titanium Nitride Multi-Layer Thin Film, 20th Int. Conf. Des. Theory Methodol. Second Int. Conf. Micro- Nanosyst., ASME Vol. 4 (2008) 539–542, doi:10.1115/DETC2008-49821.
- [24] M.P. Manoharan, A.V. Desai, M.A. Haque, Fracture toughness characterization of advanced coatings, *J. Micromechanics Microengineering* 19 (2009) 115004, doi:10.1088/0960-1317/19/11/115004.
- [25] R. Hahn, M. Bartosik, R. Soler, C. Kirchlechner, G. Dehm, P.H. Mayrhofer, Super-lattice effect for enhanced fracture toughness of hard coatings, *Scr. Mater.* 124 (2016) 67–70, doi:10.1016/j.scriptamat.2016.06.030.
- [26] H. Wang, H. Zeng, Q. Li, J. Shen, Superlattice supertoughness of TiN/MN (M = V, Nb, Ta, Mo, and W): First-principles study, *Thin Solid Films* 607 (2016) 59–66, doi:10.1016/j.ts.2016.03.061.
- [27] R. Daniel, M. Meindlhuber, J. Zalesak, B. Sartory, A. Zeilinger, C. Mitterer, J. Keckes, Fracture toughness enhancement of brittle nanostructured materials by spatial heterogeneity: A micromechanical proof for CrN/Cr and TiN/SiO<sub>x</sub> multilayers, *Mater. Des.* 104 (2016) 227–234, doi:10.1016/j.matdes.2016.05.029.
- [28] R. Hahn, N. Koutná, T. Wójcik, A. Davydok, S. Kolozsvári, C. Krywka, D. Holec, M. Bartosik, P.H. Mayrhofer, Mechanistic study of superlattice-enabled high toughness and hardness in Mo/N/Ta/Li coatings, *Commun. Mater.* 1 (2020) 62, doi:10.1038/s43246-020-00064-4.
- [29] R. Hahn, M. Bartosik, M. Arndt, P. Polcik, P.H. Mayrhofer, Annealing effect on the fracture toughness of CrN/TiN superlattices, *Int. J. Refract. Met. Hard Mater.* 71 (2018) 352–356, doi:10.1016/j.jrmhm.2017.11.008.
- [30] J. Buchinger, N. Koutná, Z. Chen, Z. Zhang, P.H. Mayrhofer, D. Holec, M. Bartosik, Toughness enhancement in TiN/WN superlattice thin films, *Acta Mater.* 172 (2019), doi:10.1016/j.actamat.2019.04.028.
- [31] U. Helmersson, S. Todorova, S.A. Barnett, J. -E. Sundgren, L.C. Markert, J.E. Greene, Growth of single-crystal TiN/VN strained-layer superlattices with extremely high mechanical hardness, *J. Appl. Phys.* 62 (1987) 481–484, doi:10.1063/1.339770.
- [32] P.B. Mirkarimi, L. Hultman, S.A. Barnett, Enhanced hardness in lattice-matched single-crystal TiN<sub>0.6</sub>Nb<sub>0.4</sub>N superlattices, *Appl. Phys. Lett.* 57 (1990) 2654–2656, doi:10.1063/1.104189.
- [33] X. Chu, S.A. Barnett, Model of superlattice yield stress and hardness enhancements, *J. Appl. Phys.* 77 (1995) 4403–4411, doi:10.1063/1.359467.

- [34] Z. Chen, D. Holec, M. Bartosik, P.H. Mayrhofer, Z. Zhang, Crystallographic orientation dependent maximum layer thickness of cubic AlN in CrN/AlN multilayers, *Acta Mater.* 168 (2019) 190–202, doi:10.1016/j.actamat.2019.02.004.
- [35] N. Koutná, R. Hahn, J. Zálešák, M. Friák, M. Bartosik, J. Keckes, M. Šob, P.H. Mayrhofer, D. Holec, Point-defect engineering of MoN/TaN superlattice films: A first-principles and experimental study, *Mater. Des.* 186 (2020) 108211, doi:10.1016/j.matdes.2019.108211.
- [36] N. Koutná, P. Rehák, Z. Chen, M. Bartosik, M. Fallmann, M. Černý, Z. Zhang, M. Friák, M. Šob, P.H. Mayrhofer, D. Holec, Correlating structural and mechanical properties of AlN/TiN superlattice films, *Scr. Mater.* 165 (2019) 159–163, doi:10.1016/j.scriptamat.2019.02.021.
- [37] M. Fallmann, Z. Chen, Z.L. Zhang, P.H. Mayrhofer, M. Bartosik, Mechanical properties and epitaxial growth of TiN/AlN superlattices, *Surf. Coatings Technol.* 375 (2019) 1–7, doi:10.1016/j.surfcoat.2019.07.003.
- [38] J. Lin, J.J. Moore, B. Mishra, M. Pinkas, X. Zhang, W.D. Sproul, CrN/AlN superlattice coatings synthesized by pulsed closed field unbalanced magnetron sputtering with different CrN layer thicknesses, *Thin Solid Films* 517 (2009) 5798–5804, doi:10.1016/j.tsf.2009.02.136.
- [39] P.E. Hovsepian, W.D. Münz, in: Recent progress in large-scale production of nanoscale multilayer/superlattice hard coatings, Elsevier Ltd, Vacuum, 2002, pp. 27–36, doi:10.1016/S0042-207X(02)00305-6.
- [40] P.H. Mayrhofer, P.E. Hovsepian, C. Mitterer, W.D. Münz, Calorimetric evidence for frictional self-adaptation of TiAlN/VN superlattice coatings, *Surf. Coatings Technol.* 177–178 (2004) 341–347, doi:10.1016/j.surfcoat.2003.09.024.
- [41] S. Gallegos-Cantú, M.A.L. Hernandez-Rodriguez, E. García-Sánchez, A. Juarez-Hernandez, J. Hernandez-Sandoval, R. Cue-Sampedro, Tribological study of TiN monolayer and TiN/CrN (multilayer and superlattice) on Co-Cr alloy, *Wear* 330–331 (2015) 439–447, doi:10.1016/j.wear.2015.02.010.
- [42] Y.X. Ou, H.Q. Wang, B. Liao, M.K. Lei, X.P. Ouyang, Tribological behaviors in air and seawater of CrN/TiN superlattice coatings irradiated by high-intensity pulsed ion beam, *Ceram. Int.* 45 (2019) 24405–24412, doi:10.1016/j.ceramint.2019.08.162.
- [43] Y.P. Purandare, G.L. Robinson, A.P. Ehiasararian, P.E. Hovsepian, Investigation of High Power Impulse Magnetron Sputtering deposited nanoscale CrN/NbN multilayer coating for tribocorrosion resistance, *Wear* 452–453 (2020) 203312, doi:10.1016/j.wear.2020.203312.
- [44] J.J. Vlassak, W.D. Nix, Measuring the elastic properties of anisotropic materials by means of indentation experiments, *J. Mech. Phys. Solids.* 42 (1994) 1223–1245, doi:10.1016/0022-5096(94)90033-7.
- [45] H. Gao, M. Abbudi, D.M. Barnett, Interfacial crack-tip field in anisotropic elastic solids, *J. Mech. Phys. Solids.* 40 (1992) 393–416, doi:10.1016/S0022-5096(05)80018-3.
- [46] S.M. Han, R. Saha, W.D. Nix, Determining hardness of thin films in elastically mismatched film-on-substrate systems using nanoindentation, *Acta Mater.* 54 (2006) 1571–1581, doi:10.1016/j.actamat.2005.11.026.
- [47] W.C. Oliver, G.M. Pharr, An improved technique for determining hardness and elastic modulus using load and displacement sensing indentation experiments, *J. Mater. Res.* 7 (1992) 1564–1583, doi:10.1557/JMR.1992.1564.
- [48] A.C. Fischer-Cripps, Critical review of analysis and interpretation of nanoindentation test data, *Surf. Coatings Technol.* 200 (2006) 4153–4165, doi:10.1016/j.surfcoat.2005.03.018.
- [49] D. Di Maio, S.G.G. Roberts, D. Di Maio, S.G.G. Roberts, Measuring fracture toughness of coatings using focused-ion-beam-machined microbeams, *J. Mater. Res.* 20 (2005) 299–302, doi:10.1557/JMR.2005.0048.
- [50] C.E. Athanasiou, H. Zhang, C. Ramirez, J. Xi, T. Baba, X. Wang, W. Zhang, N.P. Padture, I. Szlufarska, B.W. Sheldon, High toughness carbon-nanotube-reinforced ceramics via ion-beam engineering of interfaces, *Carbon N.Y.* 163 (2020) 169–177, doi:10.1016/j.carbon.2020.02.075.
- [51] X. Liu, C.E. Athanasiou, N.P. Padture, B.W. Sheldon, H. Gao, A machine learning approach to fracture mechanics problems, *Acta Mater.* 190 (2020) 105–112, doi:10.1016/j.actamat.2020.03.016.
- [52] L. Zhou, D. Holec, P.H. Mayrhofer, First-principles study of elastic properties of cubic Cr<sub>1-x</sub>Al<sub>x</sub>N alloys, *J. Appl. Phys.* 113 (2013) 043511, doi:10.1063/1.4789378.
- [53] O.A. Bauchau, J.I. Craig, in: Euler-Bernoulli beam theory, Springer, Dordrecht, 2009, pp. 173–221, doi:10.1007/978-90-481-2516-6\_5.
- [54] C.M. Wang, J.N. Reddy, K.H. Lee, Bending of Beams, in: Shear Deform. Beams Plates, Elsevier Science Ltd, 2000: pp. 11–38. doi:10.1016/b978-008043784-2/50002-2.
- [55] A. Wagner, D. Holec, P.H. Mayrhofer, M. Bartosik, Enhanced fracture toughness in ceramic superlattice thin films: on the role of coherency stresses and misfit dislocations, To Be Submitt (2020) <http://arxiv.org/abs/2008.13652>. (accessed September 1, 2020).
- [56] F.C. Frank, J.H. Van Der Merwe, N.F. Mott, One-dimensional dislocations. II. Misfitting monolayers and oriented overgrowth, *Proc. R. Soc. London. Ser. A. Math. Phys. Sci.* 198 (1949) 216–225, doi:10.1098/rspa.1949.0096.
- [57] J.W. Matthews, A.E. Blakeslee, Defects in epitaxial multilayers: I. Misfit dislocations, *J. Cryst. Growth.* 27 (1974) 118–125, doi:10.1016/S0022-0248(74)80055-2.
- [58] D. Holec, M. Friák, J. Neugebauer, P.H. Mayrhofer, Trends in the elastic response of binary early transition metal nitrides, *Phys. Rev. B.* 85 (2012) 064101, doi:10.1103/PhysRevB.85.064101.
- [59] H.J. McSkimin, P. Andreatch, Elastic moduli of silicon vs hydrostatic pressure at 25.0°C and -195.8°C, *J. Appl. Phys.* 35 (1964) 2161–2165, doi:10.1063/1.1702809.
- [60] J.J. Hall, Electronic effects in the elastic constants of n-type silicon, *Phys. Rev.* 161 (1967) 756–761, doi:10.1103/PhysRev.161.756.
- [61] H.F. Bueckner, Novel principle for the computation of stress intensity factors, *Z Angew Math Mech* 50 (1970) 529–546.
- [62] J.R. Rice, Weight Function Theory for Three-Dimensional Elastic Crack Analysis, in: R.P. Wei, R.P. Gangloff (Eds.), *Fract. Mech. Perspect. Dir. (Twentieth Symp.)*, ASTM International, 1989, pp. 29–57, doi:10.1520/STP18819S. West Conshohocken, PA.
- [63] J.R. Rice, First-order variation in elastic fields due to variation in location of a planar crack front, *J. Appl. Mech. Trans. ASME* 52 (1985) 571–579, doi:10.1115/1.3169103.
- [64] H. Gao, J.R. Rice, Nearly circular connections of elastic half spaces, *J. Appl. Mech. Trans. ASME* 54 (1987) 627–634, doi:10.1115/1.3173080.
- [65] H. Gao, J.R. Rice, Shear stress intensity factors for a planar crack with slightly curved front, *J. Appl. Mech. Trans. ASME* 53 (1986) 774–778, doi:10.1115/1.3171857.
- [66] T. Fett, Stress intensity factors and weight functions for the edge cracked plate calculated by the boundary collocation method, (1990). [https://inis.iaea.org/search/search.aspx?orig\\_q=RN:22031096](https://inis.iaea.org/search/search.aspx?orig_q=RN:22031096) (accessed March 22, 2019).
- [67] M. Bartosik, D. Holec, D. Apel, M. Klaus, C. Genzel, J. Keckes, M. Arndt, P. Polcik, C.M. Koller, P.H. Mayrhofer, Thermal expansion of Ti-Al-N and Cr-Al-N coatings, *Scr. Mater.* 127 (2017) 182–185, doi:10.1016/j.scriptamat.2016.09.022.
- [68] O. Kolednik, J. Predan, F.D. Fischer, P. Fratzl, Bioinspired design criteria for damage-resistant materials with periodically varying microstructure, *Adv. Funct. Mater.* 21 (2011) 3634–3641, doi:10.1002/adfm.201100443.
- [69] W.J. Wolfgang, Chemical analysis techniques for failure analysis: Part 1, common instrumental methods, in: *Handb. Mater. Fail. Anal. with Case Stud. from Aerosp., Automot. Ind.*, Elsevier Inc., 2016, pp. 279–307, doi:10.1016/B978-0-12-800950-5.00014-4.
- [70] F. Tessier, Determining the Nitrogen Content in (Oxy)Nitride Materials, *Materials (Basel)* 11 (2018) 1331, doi:10.3390/ma11081331.
- [71] P.H. Mayrhofer, H. Willmann, A.E. Reiter, Structure and phase evolution of Cr-Al-N coatings during annealing, *Surf. Coatings Technol.* 202 (2008) 4935–4938, doi:10.1016/j.surfcoat.2008.04.075.
- [72] P.H. Mayrhofer, D. Music, T. Reeswinkel, H.G. Fuß, J.M. Schneider, Structure, elastic properties and phase stability of Cr<sub>1-x</sub>Al<sub>x</sub>N, *Acta Mater.* 56 (2008) 2469–2475, doi:10.1016/j.actamat.2008.01.054.
- [73] P.C. Yashar, W.D. Sproul, Nanometer scale multilayered hard coatings, *Vacuum* 55 (1999) 179–190, doi:10.1016/S0042-207X(99)00148-7.
- [74] E.E. Fullerton, I.K. Schuller, H. Vanderstraeten, Y. Bruynserae, Structural refinement of superlattices from x-ray diffraction, *Phys. Rev. B.* 45 (1992) 9292–9310, doi:10.1103/PhysRevB.45.9292.
- [75] J.O. Kim, J.D. Achenbach, P.B. Mirkarimi, M. Shinn, S.A. Barnett, Elastic constants of single-crystal transition-metal nitride films measured by line-focus acoustic microscopy, *J. Appl. Phys.* 72 (1992) 1805–1811, doi:10.1063/1.351651.
- [76] P. Sharma, S. Ganti, On the grain-size-dependent elastic modulus of nanocrystalline materials with and without grain-boundary sliding, *J. Mater. Res.* 18 (2003) 1823–1826, doi:10.1557/JMR.2003.0253.
- [77] P. Valat-Villain, J. Durinck, P.O. Renault, Grain Size Dependence of Elastic Moduli in Nanocrystalline Tungsten, *J. Nanomater.* (2017) 3620910 2017, doi:10.1155/2017/3620910.
- [78] K.O. Kese, Z.C. Li, B. Bergman, Influence of residual stress on elastic modulus and hardness of soda-lime glass measured by nanoindentation, *J. Mater. Res.* 19 (2004) 3109–3119, doi:10.1557/JMR.2004.0404.
- [79] Q.N. Meng, M. Wen, C.Q. Hu, S.M. Wang, K. Zhang, J.S. Lian, W.T. Zheng, Influence of the residual stress on the nanoindentation-evaluated hardness for zirconiumnitride films, *Surf. Coatings Technol.* 206 (2012) 3250–3257, doi:10.1016/j.surfcoat.2012.01.021.
- [80] W.M. Seidl, M. Bartosik, S. Kolozsvári, H. Bolvardi, P.H. Mayrhofer, Influence of coating thickness and substrate on stresses and mechanical properties of (Ti,Al,Ta)N/(Al,Cr)N multilayers, *Surf. Coatings Technol.* 347 (2018) 92–98, doi:10.1016/j.surfcoat.2018.04.060.
- [81] K.M. Hubbard, T.R. Jervis, P.B. Mirkarimi, S.A. Barnett, Mechanical properties of epitaxial TiN/(V0.6Nb0.4)N superlattices measured by nanoindentation, *J. Appl. Phys.* 72 (1992) 4466–4468, doi:10.1063/1.352177.
- [82] S. Barnett, A. Madan, Superhard superlattices, *Phys. World.* 11 (1998) 45.
- [83] R. Pippan, S. Würster, D. Kiener, Fracture mechanics of micro samples: Fundamental considerations, *Mater. Des.* 159 (2018) 252–267, doi:10.1016/j.matdes.2018.09.004.
- [84] S. Massl, W. Thomma, J. Keckes, R. Pippan, Investigation of fracture properties of magnetron-sputtered TiN films by means of a FIB-based cantilever bending technique, *Acta Mater.* 57 (2009) 1768–1776, doi:10.1016/j.actamat.2008.12.018.
- [85] F. Iqbal, J. Ast, M. Göken, K. Durst, In situ micro-cantilever tests to study fracture properties of NiAl single crystals, *Acta Mater.* 60 (2012) 1193–1200, doi:10.1016/j.actamat.2011.10.060.
- [86] Y.Q. Wang, R. Fritz, D. Kiener, J.Y. Zhang, G. Liu, O. Kolednik, R. Pippan, J. Sun, Fracture behavior and deformation mechanisms in nanolaminated crystalline/amorphous micro-cantilevers, *Acta Mater.* 180 (2019) 73–83, doi:10.1016/j.actamat.2019.09.002.
- [87] A.K. Saxena, S. Brinckmann, B. Völker, G. Dehm, C. Kirchlechner, Experimental conditions affecting the measured fracture toughness at the microscale: Notch geometry and crack extension measurement, *Mater. Des.* 191 (2020) 108582, doi:10.1016/j.matdes.2020.108582.